Proceedings of Global Power and Propulsion Society
ISSN-Nr: 2504-4400
GPPS Hong Kong 2023
October 17-19, 2023
www.gpps.global

GPPS-TC-2023-0086

Numerical Studies on Shock Wave and Boundary Layer Interaction in the High-Load Turbine Rotor Cascades

Qiyun Long
Beijing Institute of Technology
3120210457@bit.edu.cn
Haidian District, Beijing, China

Mingxu Qi
Beijing Institute of Technology
qimx@bit.edu.cn
Haidian District, Beijing, China

Zhengxin Ji
Beijing Institute of Technology
3120210471@bit.edu.cn
Haidian District, Beijing, China

Hong Zhang
Beijing Institute of Technology
zhanghong@bit.edu.cn
Haidian District, Beijing, China

ABSTRACT

Design of transonic high-load turbine is the essential approach to improve thrust-to-weight ratio of gas turbine engines. The shock wave and boundary layer interaction (SWBLI) in high-load turbine is one of the important unsteady sources and the main source of loss in turbine stages. In order to study mechanism of SWBLI in high-load turbine, rotor blades with loading coefficients range from 1.6 to 2 were designed and Delayed Detached Eddy Simulations (DDES) were carried out. The influences of loading coefficient, exit isentropic Mach number and incidence angle on characteristics of shock wave, SWBLI as well as flow details in the blade passages were compared. Results indicated the shock wave was generated and enhanced as exit isentropic Mach number increased leading to the increase of 0.028 in the total pressure loss coefficient. The total pressure loss coefficient reached the maximum at the loading coefficient of 2.0, however it did not increase with the load coefficient because of the stronger shock wave at the loading coefficient of 1.6. Meanwhile, the influences of strong separation induced by variation of incidence angle on the fore part of suction surface of blade on the characteristics of the shock wave and the loss were also obvious.

INTRODUCTION

Gas turbine engines are one of the most dominant aero power units today. With the development of aero engines, the design requirements for thrust-to-weight ratio keep increasing (Badran, 1999). In order to increase the thrust-to-weight ratio, the turbines continue to develop towards high-load, transonic and large expansion ratio, which inevitably results in higher exit Mach number, the formation of strong shock wave, and the SWBLI (Lo, 2017). These unsteady phenomena reduce the efficiency of turbine and increase risk of fatigue and thermal failure. Therefore, it is necessary to study the interaction mechanism and regulation mechanism between shock wave and boundary layer in transonic high-load turbine.

The SWBLI was widely distributed in outer and inner flows of supersonic aircrafts. The thickness of boundary layer was increased and the separation of boundary layer could happen by the SWBLI resulting in the increase of flow loss and decrease of stability . Mechanism of SWBLI was investigated by experiment, numerical simulation and theoretical analysis since SWBLI was first discovered in 1930s and more details were found with the development of numerical simulation method. Some reviews (Dolling, 2001; Babinsky and Harvey, 2011; Gaitonde, 2013) summarized the current state of knowledge about SWBLI. In order to decrease the influence of SWBLI on performance of supersonic aircrafts, control methods of SWBLI were concerned and investigated. Depending on whether the control device is adjustable, the control methods for SWBLI could be divided into passive control and active control, including vortex generators (Titchener, 2013), bump (Zhang et al., 2019), boundary layer bleed (Bagheri, 2021), plasma actuation (Yang, 2022) and other control methods. These control methods were proven effective in specific situations.

For turbine, the SWBLI was also investigated because it was common in high-load turbine as a result of the high Mach number and the formation of the shock waves. The SWBLI over the neighboring vane and the downstream row resulted in significant efficiency reduction and high cycle fatigue (Paniagua et al., 2008). Bian et al. (2019) studied the interaction mechanisms of shock wave with the boundary layer and wake in the high-load nozzle guide vane by hybrid RANS/LES.

The results showed that strong shock waves induced boundary layer separation, while the presence of the separation bubble could in turn lead to a Mach reflection phenomenon. Sonoda et al. (2006; 2009) systematically studied the influence of local geometric optimization on turbine flow losses. The results found that local geometric optimization of the suction surface profile of the guide vane could change the flow condition of the boundary layer, control the effect of SWBLI by changing one strong reflection shock wave into two weak reflection shock waves. Based on the same idea, Lei (2017) and Zhao (2019) controlled flow condition of boundary layer and changed the features of SWBLI by grooved vane. There were some studies on the mechanism and control method of SWBLI in high-load turbine but the mechanism of SWBLI in high-load turbine need further studies because of the unsteadiness of SWBLI in order to prepare for study on control method of SWBLI to increase the efficiency and the stability.

In the present work, rotor blades with loading coefficients range from 1.6 to 2 were designed and the simulations of cascade were carried out by DDES to observe the influence of the loading coefficient, the exit isentropic Mach number and the incidence angle on the structure of shock wave and SWBLI.

METHODOLOGY

Investigated Model

The design of rotor blade was based on the rotor blade of TTM-Stage (Erhard, 2000). Significant changes to the rotor blade of TTM-Stage were performed in order to achieve the high loading coefficient. The key geometry parameters of the blade in the cascade with the loading coefficient of 2.0 are listed in Table 1. The other blades with smaller loading coefficient were obtained by modifying turning angle based on the blade with the loading coefficient of 2.0.

Table 1. Geometry parameters of the blade in the cascade

Parameters	Value
Chord (mm)	54.78
Pitch (mm)	29.5
Height (mm)	15
Inlet vane angle (deg)	48.97
Outlet vane angle (deg)	62.36

Numerical Method

For DDES, the SA-DDES model was employed to deal with the turbulent flow in time-dependent Navier-Stokes equations using the solver embedded into NUMECA software package. The DDES model provided additional shielding functions to ensure that the model does not switch to Large eddy simulation (LES) within the boundary layer in order to avoid the limitation of high sensitivity to grid spacing. The dual time stepping approach proposed was employed. At each physical time step, a steady-state problem was solved in a pseudo time. In order to speed up the convergence, the multigrid strategy and the implicit residual smoothing method were applied.

Boundary Condition

The total pressure, the total temperature and the velocity vector on the inlet boundary were specified. The Mach number was obtained by extrapolation from the interior field. At the outlet boundary, the static pressure was specified. The remaining dependent variables at the outlet boundary were obtained from the interior field through the extrapolation with the zero-order.

Computational Mesh

The grid was generated by the Autogrid5 module of the NUMECA software. The grid independence study was performed to confirm the reliability of the numerical simulation and the Grid independence results is shown in Figure 1. The total pressure ratio represented the ratio of the outlet total pressure to inlet total pressure. The number of 9 million grids was determined for calculation based on calculation accuracy and calculation time. Figure 2 shows the grids of the blade in cascade. The first layer grid scale was $5x10^{-6}$ meter and the average y+ value was about 1. The physical time step was set to $1x10^{-6}$ second.

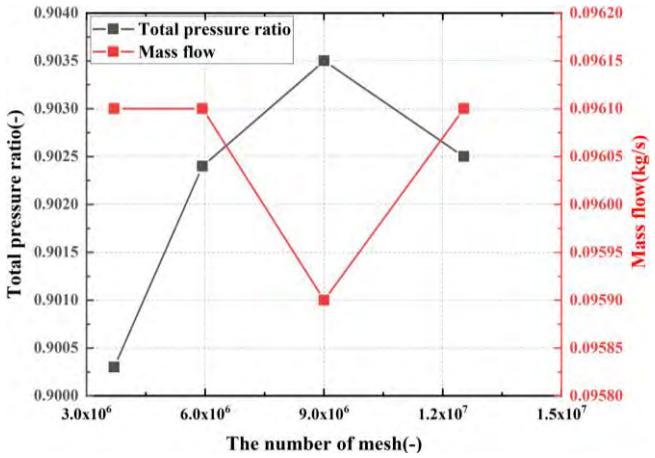

Figure 1 Grid independence results

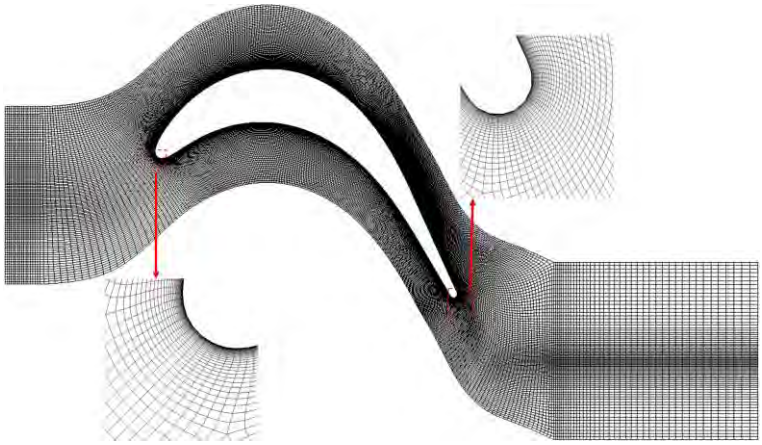

Figure 2 B2B computational mesh

Convergence

The steady calculation was carried out with 400 iterations and the DDES calculation was carried out with 350 iterations to ensure the convergence of the results. The initial condition of the DDES calculation was based on the result of the steady calculation. Figure 3 shows the root mean square global residual of the density of the RANS calculation reached 10^{-5} at the exit isentropic Mach number of 0.9 and the incidence angle of 0 for the blade with the loading coefficient of 2.0. The definition of the residual was the sum of the fluxes on all the faces of each cell and the data shown in Figure 3 was the logarithm of the root mean square global residual. The convergence of other conditions were similar with the convergence shown in Figure 3. The highest error in inlet mass flow and outlet mass flow was less than 0.05% and the global residual was more than 10^{-5} for the DDES results of all conditions.

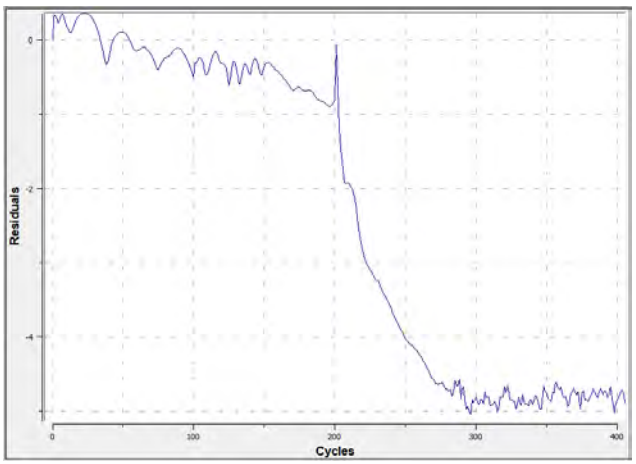

Figure 3 The global residual of the RANS calculation at the exit isentropic Mach number of 0.9 and the incidence angle of 0 for the blade with the loading coefficient of 2.0

RESULTS AND DISCUSSION

Comparison of Flow Fields with Different Exit Isentropic Mach Number

Figure 4 shows the total pressure loss coefficient at exit at loading coefficient of 2.0 and incidence angle of 0° with different exit isentropic Mach number. The total pressure loss coefficient is expressed by Equation (1)

$$\omega = \frac{P_0^* - P^*}{P_0^*} \qquad (1)$$

Where P_0^* is the inlet total pressure, P^* is the local total pressure.

The exit isentropic Mach number is expressed by Equation (2).

$$M_{exit}^{isentropic} = \sqrt{\left(\left(\frac{P_0^{freestream}}{P_1} \right)^{\frac{\gamma-1}{\gamma}} - 1 \right) \times \frac{2}{\gamma - 1}} \qquad (2)$$

Where $P_0^{freestream}$ is the total pressure in the freestream outside of the boundary layers, usually the inlet total pressure is used, P_1 is the exit static pressure and γ is the ratio of specific heat, which is 1.4 for air. When the exit static pressure is determined, the exit isentropic Mach number is changed by changing the inlet total pressure.

As Figure 4 shown, the total pressure loss coefficient increases with the increase of exit isentropic Mach number because of the higher flow velocity and the formation of the shock wave. Figure 5 shows the total pressure loss coefficient along pitch at exit of mid-span with different exit isentropic Mach number. The total pressure loss coefficient shows the similar distribution when the exit isentropic Mach number increases from 0.9 to 1.1. There is a high loss region at 0.87 pitch corresponding to the wake where the loss rises from 0.105 to 0.166. At the exit isentropic Mach number of 1.2, the distribution of the total pressure loss coefficient is different from others, which is basically uniform along the pitch because the main flow and the wake are strongly blended as Figure 6 shown.

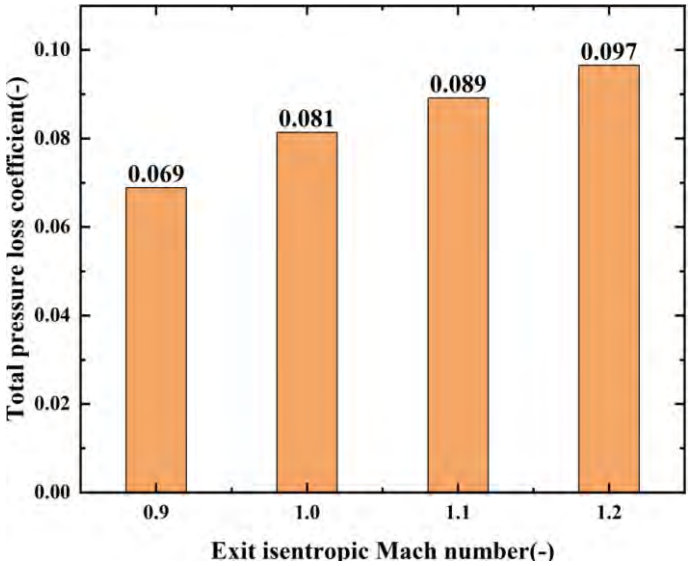

Figure 4 Total pressure loss coefficient at exit with different exit isentropic Mach number

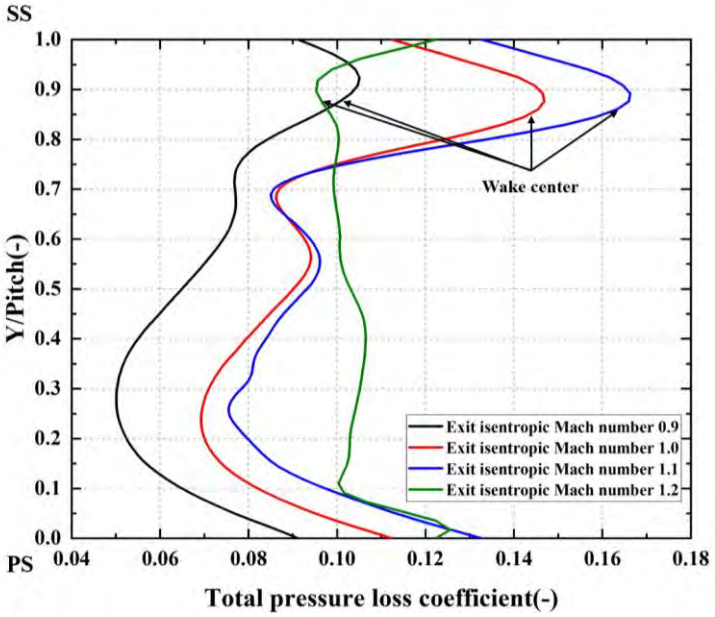

Figure 5 Total pressure loss coefficient along pitch at exit of mid-span with different exit isentropic Mach number

Figure 6 and Figure 7 show the distribution of Mach number and pressure coefficient at mid-span(Cp). The pressure coefficient is expressed by Equation (2).

$$C_p = \frac{P - P_1}{P_0^* - P_1} \qquad (2)$$

Where P is the local static pressure, P_1 is the exit static pressure and P_0^* is the inlet total pressure.

As Figure 6 shown, there is no shock wave formation at exit isentropic Mach number of 0.9. With the increase of the exit isentropic Mach number, the shock waves are generated, consisted of incident shock wave, reflected shock wave and Mach stem and the Mach number preceding the shock wave increases. The position of the shock wave at the suction surface moves towards the trailing edge and the angle between incident shock wave and reflected shock wave increases.

With the increase of exit isentropic Mach number, the sudden Cp rise in suction surface decreases in Figure 7, but the sudden static pressure rise increases according to the definition of Cp because of the difference of the inlet total pressure, which is induced by the shock wave and boundary layer interaction, indicating the intensity of the shock wave increases.

Figure 8 shows the distribution of axial skin friction coefficient (Cf_z) on the suction surface at mid-span. The axial skin friction coefficient is expressed by Equation (3).

$$C_{f_z} = \frac{\tau_{\omega_z}}{0.5\rho_{ref}V_{ref}^2} \qquad (3)$$

Where τ_{ω_z} is the local axial wall shear stress, ρ_{ref} and V_{ref} are the reference density and reference velocity, respectively, for which the average inlet density and the average inlet velocity are used.

Cf_z can be used to represent the state of the boundary layer. The Cf_z less than 0 indicates the suction surface of the blade has a backflow region. The point of separation and reattachment of the flow is represented by the Cf_z of 0, which can be used to calculate the length of the separating bubble. In Figure 8, the Cf_z increases on the suction surface indicating that the boundary layer transitions from laminar to turbulent flow. The Cf_z suddenly drops to less than zero at the location where the shock wave occurs, which means the point of separation. At various exit isentropic Mach numbers, the location of separation bubble matches that of the shock wave, which moves towards the trailing edge. There is no separation bubble formation at exit isentropic Mach number of 0.9 and the length of the separation bubble increases from 1.18% to 1.29% Cx as the exit isentropic Mach number increases from 1.0 to 1.1. However, the length of the separation bubble is 0.73% Cx at the exit isentropic Mach number of 1.2, which is less than that at lower exit isentropic Mach number. It appears to show that the length of separation bubble does not grow as the intensity of the shock wave increases. The characteristics of the separation bubble at mid-span will be influenced by the secondary flow from the endwall as the exit Mach number increases.

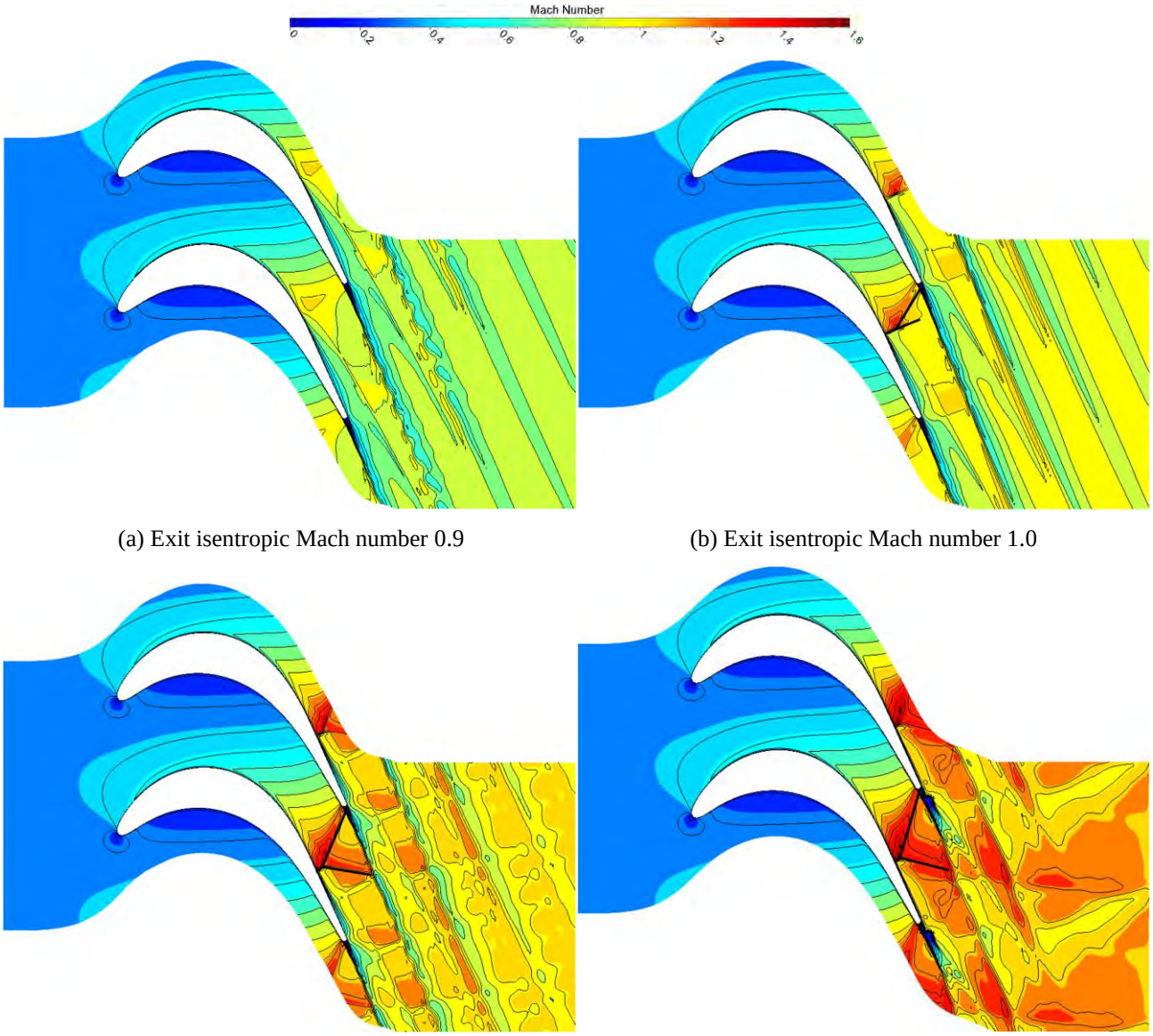

(a) Exit isentropic Mach number 0.9

(b) Exit isentropic Mach number 1.0

(c) Exit isentropic Mach number 1.1

(d) Exit isentropic Mach number 1.2

Figure 6 Mach number contour at mid-span with different exit isentropic Mach number

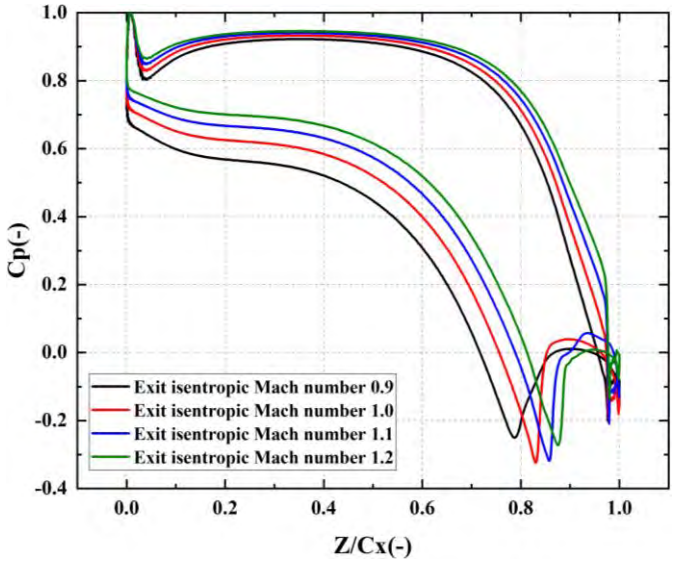

Figure 7 Distribution of Cp at mid-span with different exit isentropic Mach number

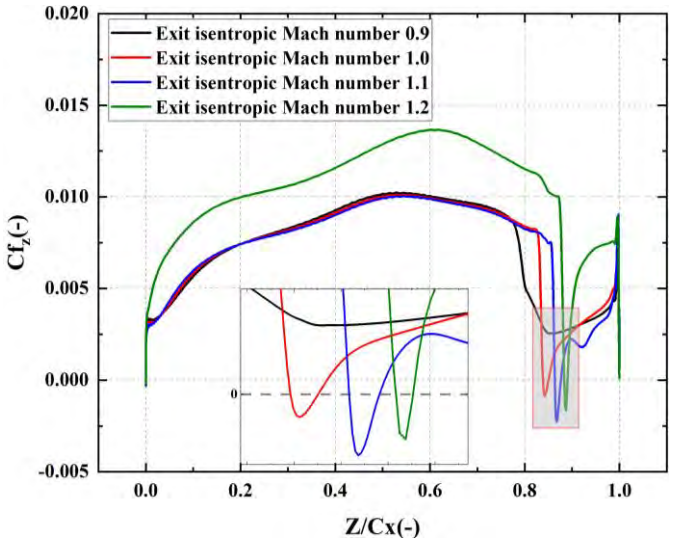

Figure 8 Distribution of Cf_z at mid-span on suction surface with different isentropic Mach number

Comparison of Flow Fields with Different Loading Coefficient

Figure 9 shows the total pressure loss coefficient at exit at exit isentropic Mach number of 1.2 and incidence angle of 0° with different loading coefficient. The total pressure loss coefficient reaches the maximum value of 0.097 at loading coefficient of 2.0 and reaches the minimum value of 0.090 at loading coefficient of 1.8. The formation of obvious vortices on the upper and lower endwalls of the suction surface at load coefficient of 1.6 leads the total pressure loss coefficient at load coefficient of 1.6 to be larger than that at load coefficient of 1.8. Figure 10 shows the total pressure loss coefficient along pitch at exit of mid-span at exit isentropic Mach number of 1.2 and incidence angle of 0° with different loading coefficient. The distribution of the total pressure loss coefficient and the position of the wake are different in Figure 10 when the loading coefficient increases from 1.6 to 2.0 because of the increase of the turning angle. There is a high loss region corresponding to the wake at load coefficient of 1.6 and 1.8 and there is another high loss region at 0.7 pitch caused by the SWBLI at load coefficient of 1.6.

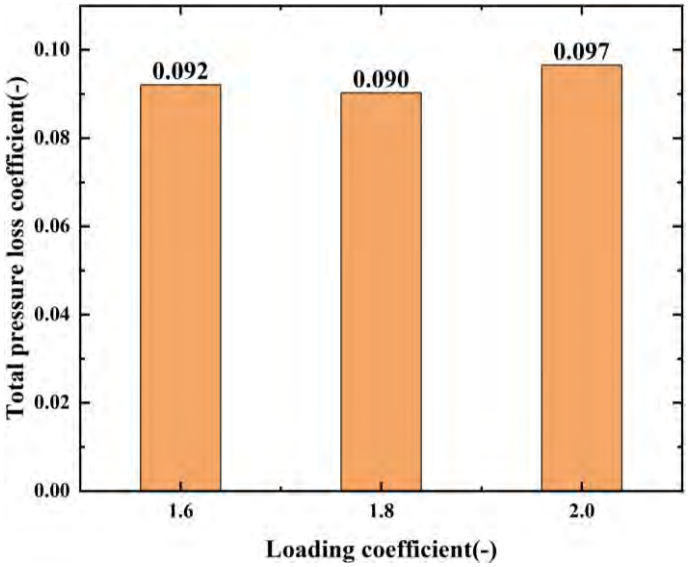

Figure 9 Total pressure loss coefficient at exit with different loading coefficient

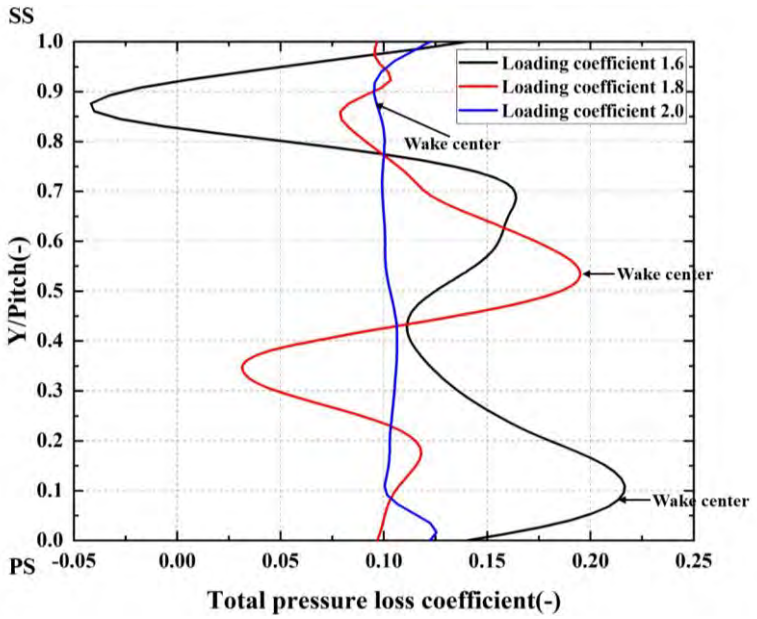

Figure 10 Total pressure loss coefficient along pitch at exit of mid-span with different loading coefficient

Figure 11 and Figure 12 show the distribution of Mach number and Cp at mid-span. With the increase of the loading coefficient, the position of the shock wave moves towards the leading edge and the interaction between the shock wave and the wake strengthens, resulting in the uniformity of outlet flow field as the Figure 11 shown. Figure 12 shows the same change of the position of the shock wave and the Cp rise induced by the shock wave. The intensity of the shock wave and the Mach number preceding the shock wave at load coefficient of 1.6 are significantly higher than those at the load factor of 1.8 and 2.0.

Figure 13 shows the distribution of Cf_z on the suction surface at mid-span. The transition at loading coefficient of 1.6 is completed earlier than that at the loading coefficient of 1.8 and 2.0. The length of the separation bubble induced by the shock wave is obviously longer than others at loading coefficient of 1.6, which leads to the higher total pressure loss coefficient at loading coefficient of 1.6 than at load factor of 1.8. With the increase of the loading coefficient, the length of the separation bubble decreases from 3.8% to 0.73% Cx.

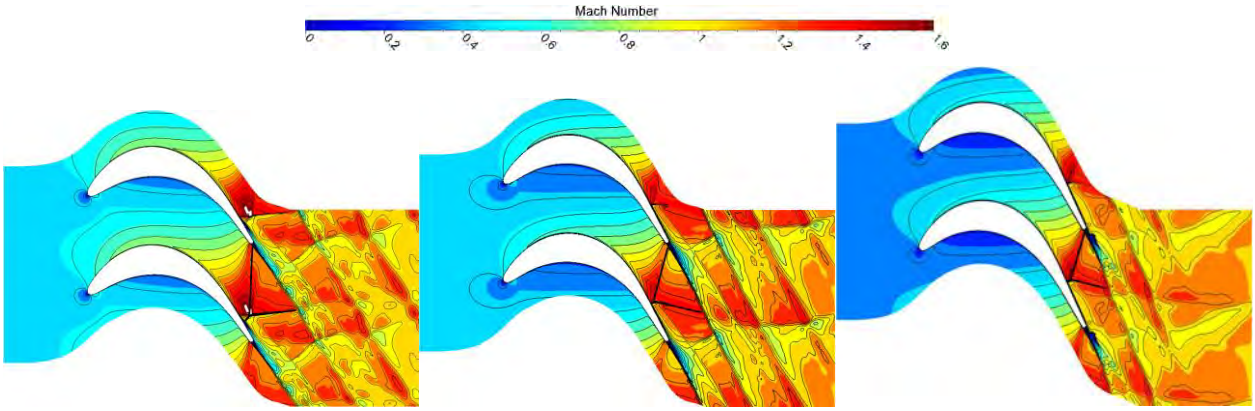

(a) loading coefficient 1.6 (b) loading coefficient 1.8 (c) loading coefficient 2.0

Figure 11 Mach number contour at mid-span with different loading coefficient

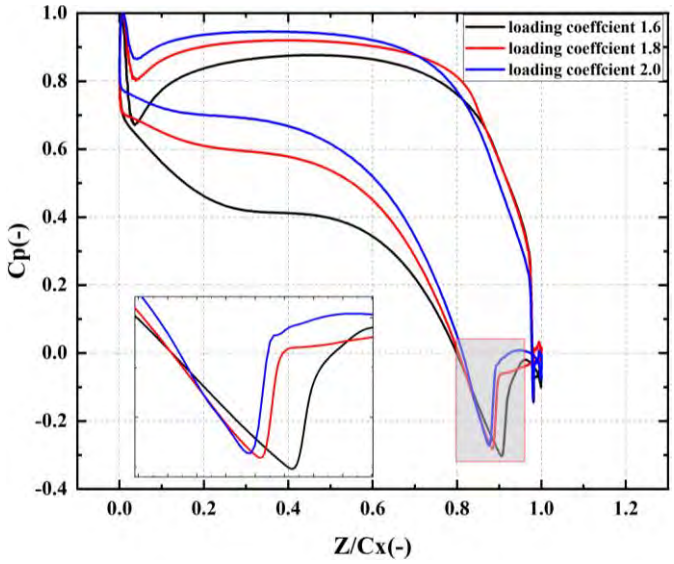

Figure 12 Distribution of Cp at mid-span with different loading coefficient

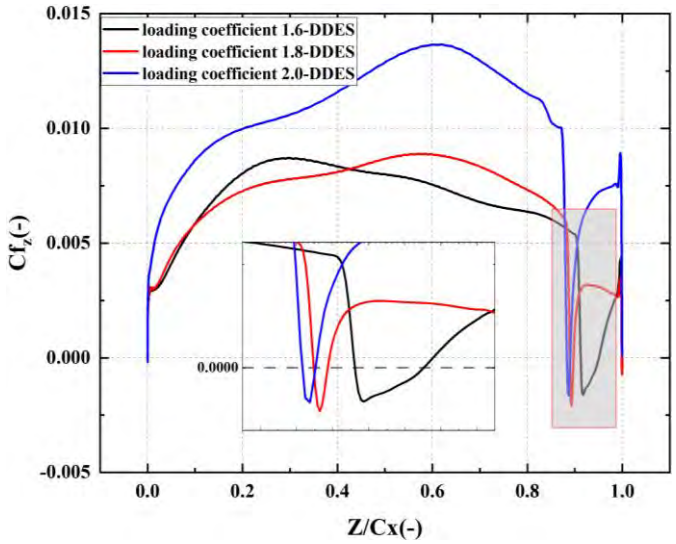

Figure 13 Distribution of Cf_z on suction surface at mid-span with different loading coefficient

Comparison of Flow Fields with Different Incidence Angle

Figure 14 shows the total pressure loss coefficient at exit at loading coefficient of 2.0 and exit isentropic Mach number of 1.2 with different incidence angle. The total pressure loss coefficient reaches the maximum of 0.119 at incidence angle of +15° and reaches the minimum of 0.091 at incidence angle of negative 7.5°, indicating the loss increase with the large positive incidence angle. Figure 15 shows the total pressure loss coefficient along pitch at exit of mid-span with different incidence angle. At the negative incidence angles, there is a high loss region at 0.94 pitch corresponding to the wake and there is another high loss region at 0.6 pitch because of the flow separation induced by the SWBLI . The distribution of the total pressure loss coefficient at incidence angle of 0° is basically uniform because of the strong blend of the main flow and the wake. There is a high loss region at 0.94 pitch corresponding to the wake at incidence angle of positive 7.5°, however, the distribution is absolutely different at incidence angle of positive 15°. The high loss area is generated by separated flow from the suction surface, not by the wake.

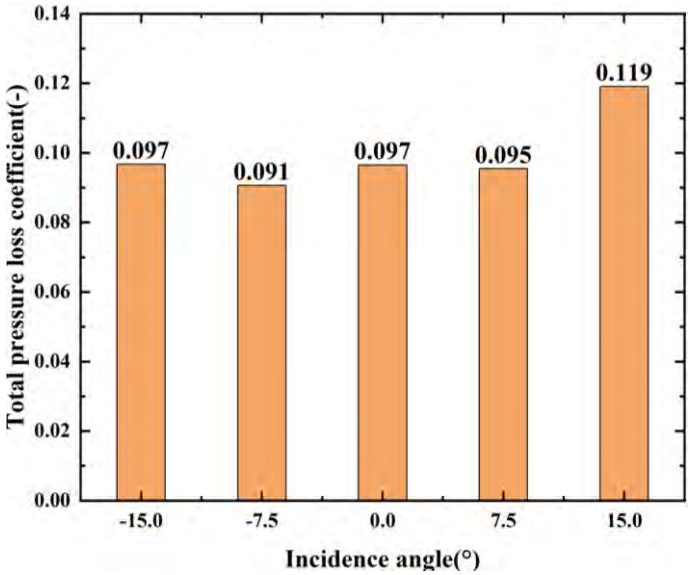

Figure 14 Total pressure loss coefficient at exit with different incidence angle

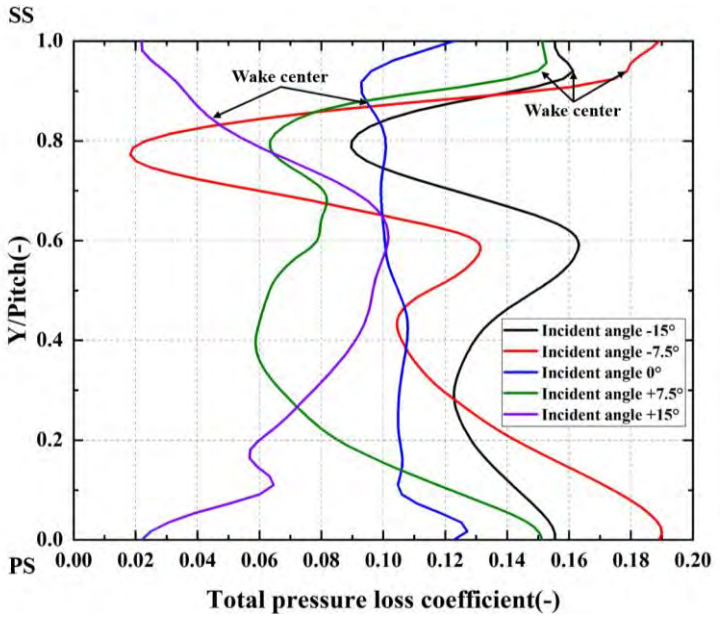

Figure 15 Total pressure loss coefficient along pitch at exit of mid-span with different incidence angle

Figure 16 and Figure 17 show the distribution of Mach number and Cp at mid-span. There is a large flow separation on pressure surface at incidence angle of -15° and a large flow separation on suction surface at incidence angle of +15°. The large flow separation on pressure surface do not influence the trailing edge shock wave, therefore the shock waves and the loss are basically the same at incidence angle of 0° and negative incidence angle. There is the shock wave at the leading edge of the suction surface at incidence angle of +15° resulting in the large flow separation, the bending of the shock wave at the trailing edge and the increase of the loss. The intensity of the wake and the interaction between the shock wave and the wake are reduced, leading to the different distribution of the total pressure loss coefficient as Figure 15 shown. There is not flow separation at incidence angle of +7.5°, therefore the loss is essentially unchanged.

With the variation of the incidence angle, the position and the intensity of the Cp rise induced by the shock wave are essentially the same but the intensity of the Cp rise at the incidence angle of +15° significantly increases because the shock wave is bent and is more perpendicular to the direction of the flow. Additionally, there is a Cp rise at the leading edge of the suction surface representing the formation of the shock wave.

Figure 18 shows the distribution of Cf_z on the suction surface at mid-span. The Cf_z quickly drops when the shock wave occurs on the suction surface and the separation bubble is generated except the incidence angle of +15°. At the incidence angle of +15°, the boundary layer of the suction surface influenced by the shock wave thickens but no separation bubble is generated because there is a separation bubble formation with the length of 0.8 Cx at the leading edge of the suction surface. As the flow develops, the open separation occurs following the separation bubble as the Figure 16 shown. The position of

the separation bubble is almost the same and corresponds to the position of the shock wave at other incidence angles. The length of the separation bubble is 1.11% Cx at negative incidence angle, 0.73% Cx at the incidence angle of 0° and 1.12% Cx at the incidence angle of +7.5°.

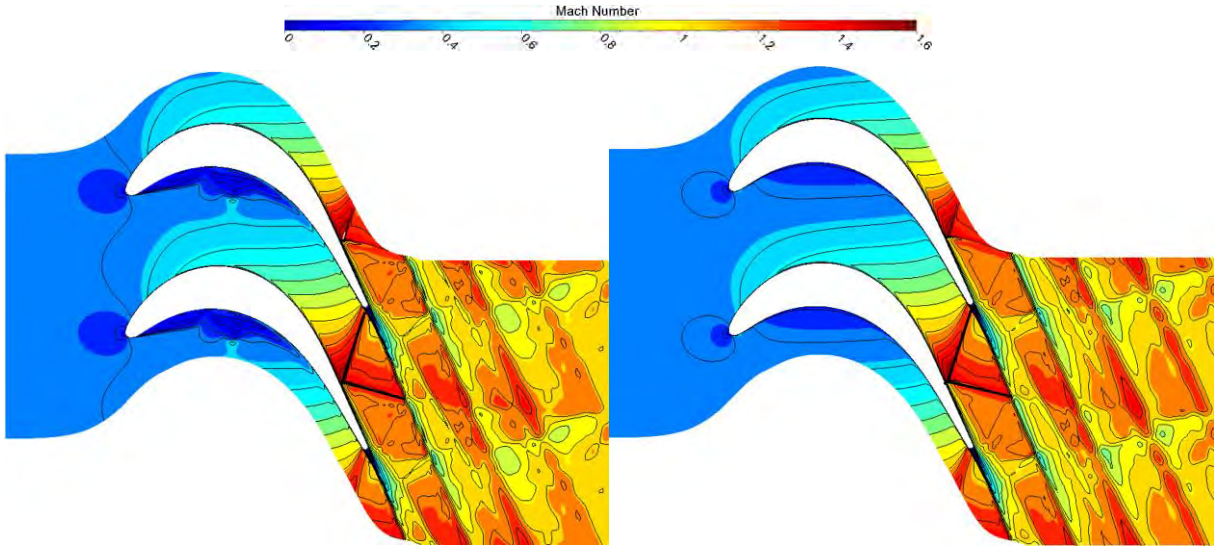

(a) Incidence angle -15°

(b) Incidence angle -7.5°

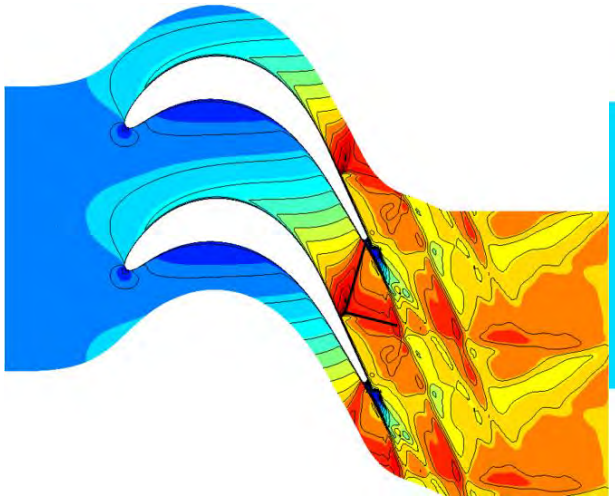

(c) Incidence angle 0°

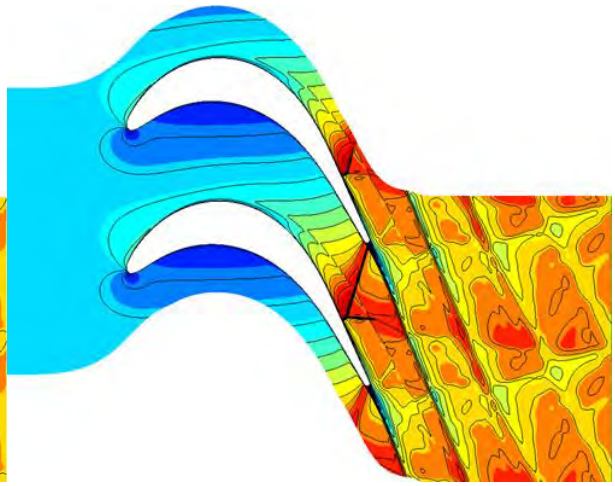

(d) Incidence angle +7.5°

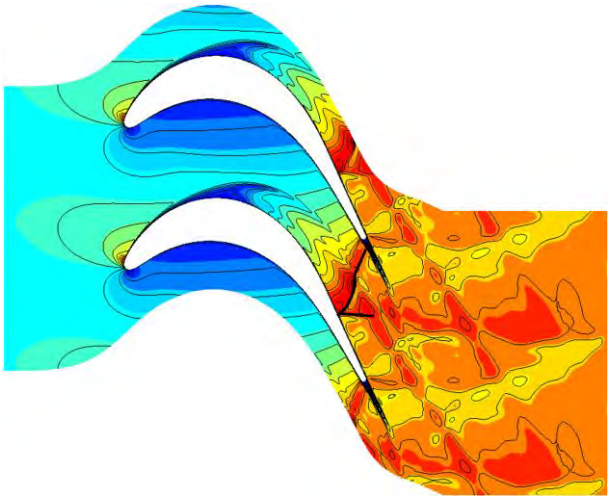

(e) Incidence angle +15°

Figure 16 Mach number contour at mid-span with different incidence angle

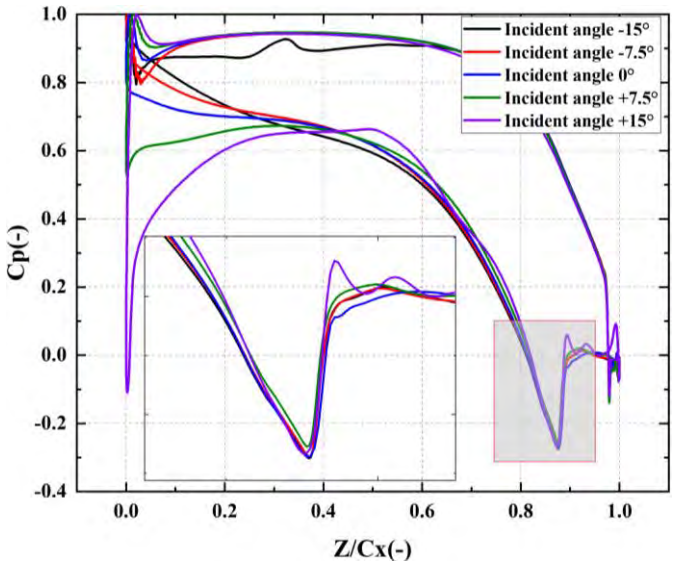

Figure 17 Distribution of Cp at mid-span with different incidence angle

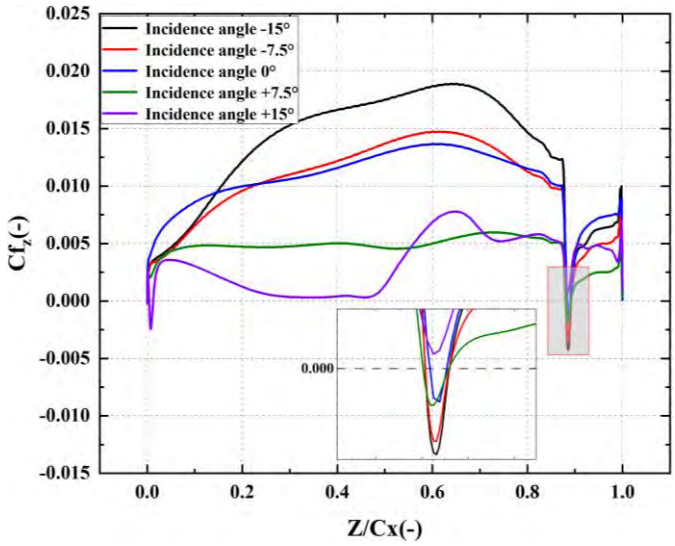

Figure 18 Distribution of Cf_z on suction surface at mid-span with different incidence angle

CONCLUSIONS

The rotor blades with high loading coefficient were designed with the aim of investigating the effects of the loading coefficient, incidence angle, and exit isentropic Mach number on the shock wave and the boundary layer interaction as well as the loss mechanism in the cascade. The research is summarized as follows.

1. With the increase of exit isentropic Mach number, the total pressure loss coefficient increases and the generated shock waves at mid-span consisted of incident shock wave, reflected shock wave and Mach stem. The position of the shock wave at the suction surface moved towards the trailing edge and the angle between incident shock wave and reflected shock wave increases. The sudden static pressure rise on suction surface induced by the shock wave increased, indicating the rise in the intensity of the shock wave. However, the length of the separation bubble did not continue to increase with the increase of exit isentropic Mach number especially at the exit isentropic Mach number of 1.2 indicating the length of separation bubble did not grow as the intensity of the shock wave increases because of the influence of the secondary flow from endwall. The distribution of total pressure loss coefficient along pitch at the exit isentropic Mach number of 1.2 was different from others indicating the main flow and the wake are strongly blended.
2. With the increase of loading coefficient, the total pressure loss coefficient reached the maximum of 0.097 at loading coefficient of 2.0 and reached the minimum of 0.090 at loading coefficient of 1.8. The position of the generated shock wave at the suction surface of mid-span moved towards the leading edge. The intensity of the shock wave and the Mach number preceding the shock wave at load coefficient of 1.6 were significantly higher

than those at the load factor of 1.8 and 2.0 leading to the longer length of the separation bubble than others and the higher total pressure loss coefficient at loading coefficient of 1.6 than that at load factor of 1.8 because of the influence of the obvious vortices on the upper and lower endwalls of the suction surface. The distribution of the total pressure loss coefficient along pitch and the position of the wake were different because of the increase of the turning angle.

3. With the variation of incidence angle, the total pressure loss coefficient reached the maximum of 0.119 at incidence angle of +15° and reached the minimum of 0.091 at incidence angle of -7.5°, indicating the loss increase with the large positive incidence angle. There was the corresponding influence on the shock wave as well as the flow field at mid-span. The position of the shock wave at the trailing edge was almost not changed at all incidence angles. At the negative incidence angles, there were the same intensity of the shock wave, the same length of the separation bubble and the same distribution of the total pressure loss coefficient along pitch. The large flow separation was generated on the fore part of the pressure surface but has no influence on loss. At the positive incidence angle, the intensity of the shock wave at the trailing edge at the incidence angle of +15° significantly increased because the shock wave is bent and is more perpendicular to the direction of the flow. The length of the separation bubble at incidence angle of +7.5° was the same as that at negative angles but there was no separation bubble formation at the position of the shock wave at the incidence angle of +15° because the large flow separation was happened on the fore part of the suction surface induced by the shock wave at the leading edge, resulting in the different distribution of total pressure loss coefficient along pitch and the increase of the loss.

NOMENCLATURE

y^+	Non-dimensional distance from the wall
P_0^*	Inlet total pressure
P^*	Local total pressure
$P_0^{freestream}$	Total pressure in the freestream outside of the boundary layers
P_1	Exit static pressure
γ	Ratio of specific heat
P	Local static pressure
τ_{ω_z}	Local axial wall shear stress
ρ_{ref}	Reference density
V_{ref}	Reference velocity

ABBREVIATIONS

SWBLI	Shock wave and boundary layer interaction
DDES	Delayed Detached Eddy Simulation
SA-DDES	Delayed Detached Eddy Simulation based on Spalart-Allmaras turbulent model
LES	Large eddy simulation
Cp	Pressure coefficient
Cf_z	Axial skin friction coefficient
Cx	Axial chord

ACKNOWLEDGMENTS

This work is supported by the National Science and Technology Major Project [J2019-II-0008-0028].

REFERENCES

Babinsky H., and Harvey J. K. (Eds.). (2011). Shock wave-boundary-layer interactions (Vol. 32). Cambridge: Cambridge University Press.

Badran O. O. (1999). Gas-turbine performance improvements. Applied Energy, 64(1-4), 263-273. https://doi.org/10.1016/S0306-2619(99)00088-4

Bagheri H., Mirjalily S. A. A., Oloomi S. A. A., and Salimpour M. R. (2021). Effects of micro-vortex generators on shock wave structure in a low aspect ratio duct, numerical investigation. Acta Astronautica, 178, 616-624. https://doi.org/10.1016/j.actaastro.2020.08.012

Bian X. T., Wang Q. S., Su X. R., and Yuan X. (2020). Interaction mechanisms of shock waves with the boundary layer and wakes in a highly-loaded NGV using hybrid RANS/LES. Chinese Journal of Aeronautics, 33(1), 149-160. https://doi.org/10.1016/j.cja.2019.07.008

Dolling D. S. (2001). Fifty years of shock-wave/boundary-layer interaction research: what next?. AIAA journal, 39(8), 1517-1531. https://doi.org/10.2514/2.1476

Erhard, J. (2000). Design, construction and commissioning of a transonic test-turbine facility. Ph.D. Graz University of Technology.

Gaitonde D. V. (2015). Progress in shock wave/boundary layer interactions. Progress in Aerospace Sciences, 72, 80-99. https://doi.org/10.1016/j.paerosci.2014.09.002

Lei X., Qi M., Sun H., and Hu L. (2017). Investigation on the shock control using grooved surface in a linear turbine nozzle. Journal of Turbomachinery, 139(12), 121008. https://doi.org/10.1115/1.4037860

Lo K. H., and Kontis K. (2017). Flow visualisation of a normal shock impinging over a rounded contour bump in a Mach 1.3 free-stream. Journal of Visualization, 20, 237-249. https://doi.org/10.1007/s12650-016-0392-4

Paniagua G., Yasa T., de la Loma A., Castillon L., and Coton T. (2008). Unsteady strong shock interactions in a transonic turbine: experimental and numerical analysis. Journal of propulsion and power, 24(4), 722-731. https://doi.org/10.2514/1.34774

Sonoda T., Arima T., Olhofer M., Sendhoff B., Kost F., and Giess P. A. (2006). A study of advanced high-loaded transonic turbine airfoils. https://doi.org/10.1115/1.2221325

Sonoda T., Hasenjäger M., Arima T., and Sendhoff B. (2009). Effect of end wall contouring on performance of ultra-low aspect ratio transonic turbine inlet guide vanes. https://doi.org/10.1115/1.2813015

Titchener N., and Babinsky H. (2013). Shock wave/boundary-layer interaction control using a combination of vortex generators and bleed. AIAA journal, 51(5), 1221-1233. https://doi.org/10.2514/1.J052079

Yang H., Zong H., Liang H., Wu Y., Zhang C., Kong Y., and Li Y. (2022). Swept shock wave/boundary layer interaction control based on surface arc plasma. Physics of Fluids, 34(8), 087119. https://doi.org/10.1063/5.0100630

Zhang Y., Tan H. J., Li J. F., and Yin N. (2019). Control of cowl-shock/boundary-layer interactions by deformable shape-memory alloy bump. AIAA Journal, 57(2), 696-705. https://doi.org/10.2514/1.J057409

Zhao B., Qi M., Sun H., Shi X., and Ma C. (2019). Experimental and numerical investigation on the shock wave structure alterations and available energy loss variations with a grooved nozzle vane. Journal of Turbomachinery, 141(5), 051001. https://doi.org/10.1115/1.4041819